A Review of Numerical Methodologies for Predicting Rotating Stall and Surge in High-Speed Centrifugal Compressors

Neri, Francesco; Hickel, Stefan; Pini, Matteo

DOI
10.1115/1.4066715

Publication date
2025

Document Version
Final published version

Published in
Journal of Engineering for Gas Turbines and Power

ASME Journal of Engineering for Gas Turbines and Power
Online journal at:
https://asmedigitalcollection.asme.org/gasturbinespower

A Review of Numerical Methodologies for Predicting Rotating Stall and Surge in High-Speed Centrifugal Compressors

Francesco Neri[1]
Propulsion and Power, Aerodynamics,
Faculty of Aerospace Engineering,
Delft University of Technology,
Delft 2629HS, The Netherlands
e-mail: f.neri@tudelft.nl

Stefan Hickel
Aerodynamics,
Faculty of Aerospace Engineering,
Delft University of Technology,
Delft 2629HS, The Netherlands
e-mail: s.hickel@tudelft.nl

Matteo Pini
Propulsion and Power,
Faculty of Aerospace Engineering,
Delft University of Technology,
Delft 2629HS, The Netherlands
e-mail: m.pini@tudelft.nl

High-speed supersonic radial compressors are a critical enabling technology for meeting the requirements of future aviation-propulsion and thermal-management systems. These turbomachines must be designed to be both efficient and robust on the widest possible operating range. Flow instabilities in the form of rotating stall and surge are therefore phenomena that must be accurately predicted early in the design process. Unsteady full-annulus computational fluid dynamics (CFD) can be used to get accurate information about the onset of instabilities, but at the expense of costly simulations. As a result, the design of new compressors continues to rely on existing correlations for the prediction of the critical mass flowrate. This approach, however, leads to suboptimal compressor designs. This article provides a review of the numerical methodologies that can be used for the accurate prediction of the critical mass flowrate in high-speed centrifugal compressors. Methods of different fidelity level and computational cost are described. Two particularly promising models, namely, those proposed by Spakovszky and Sun, are subsequently examined in more detail. Exemplary applications of these two models are finally discussed.
[DOI: 10.1115/1.4066715]

Keywords: rotating stall, surge, high-speed compressors

1 Introduction

The current trend of increasing the pressure ratio and speed in radial compressors of novel propulsion and thermal management systems can lead to compact transonic designs characterized by reduced operating range. Examples of such applications are high-speed air compressors for H_2-fed fuel cells, refrigerant cycle compressors for environmental control systems based on the vapor-compression cycle concept, and compressors for novel turboshafts of onboard power-generation systems for hybrid propulsion [1]. Operation at reduced mass flowrate is particularly severe for high-speed machines due to the occurrence of shock-wave—boundary-layer interaction phenomena and large-scale boundary layer separations that can lead to rotating stall or surge [2].

Surge consists of axisymmetric flow perturbations that lead, in the most dramatic case, to intermittent reverse flow (i.e., deep surge). Its fundamental mechanism was described by Greitzer [3], who attributed the phenomenon to the natural resonance of the compression system excited by the unsteady action of the compressor. Rotating stall is characterized by perturbations with a finite circumferential extension that propagate and evolve throughout the machine. In this condition, the compressor performance is degraded even if it continues to work steadily. Emmons [4] was the first to describe the fundamental mechanism, relating rotating stall to the flow blockage generated by a local flow separation. Under these conditions, the flow incidence of adjacent blades is altered, and the stalled lobe passes to the neighboring blades. The physical phenomenon is illustrated in Fig. 1. In most of the cases, rotating

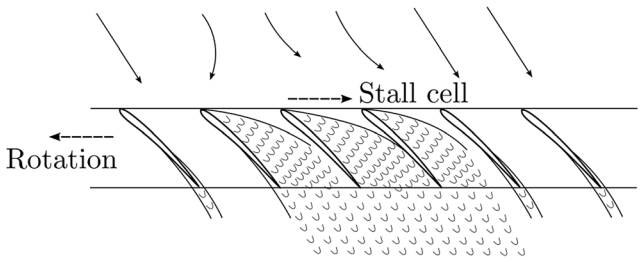

Fig. 1 Sketch of the rotating stall mechanism, adapted from Emmons et al. [4]

Turbo Expo, June 24–28, 2024. GT2024.
[1]Corresponding author.
Manuscript received September 9, 2024; final manuscript received September 17, 2024; published online October 26, 2024. Editor: Jerzy T. Sawicki.

stall eventually leads to surge, and both phenomena must be avoided for the safe and efficient operation of the compressor. In order to guarantee attached flow at all operating conditions, designers typically apply a significant safety margin. In the early design stage, such margin is estimated by means of semi-empirical correlations, and reduced later in the process through more accurate computational fluid dynamics (CFD) studies. The accurate prediction of rotating stall and surge early in the design process of compressors is therefore of paramount importance to meet the required target of operability.

Instability models have been developed over the last 80 years and reviewed, for instance, by Day [5]. Rotating stall was deeply investigated in the 1940s when it became evident that certain aircraft engines faced catastrophic failures under specific flight conditions. Compared to centrifugal machines, the flow in axial compressors undergoes similar instability mechanisms, even though the critical location is usually different [6–8]. In axial compressors, flow instabilities usually originate at the blade tip of the first stage, where the blade loading is at its maximum. In radial machines, the diffuser is usually the most critical component, where the low momentum flow in the boundary layer tends to reverse its direction due to the adverse pressure gradient.

In spite of the many studies, there is not yet consensus in the research community on whether the critical mass flowrate must be set on stall or surge. Many authors suggest that rotating low-amplitude waves are always the main inception mechanism for both stall and surge. In their experimental campaigns, Camp and Day [9], Tryfonidis et al. [10], and Garnier et al. [11] showed that these waves always occurred before any rotating stall or surge event. They noticed that these prestall waves can be distinguished into two different types:

- long-wavelength, or modal-waves, which are characterized by a circumferential extension of the same order of magnitude of the machine diameter, and their growth process spans several rotor revolutions;
- short-wavelength, or spike-waves, whose length scale is that of the blade pitch, and their growth process saturates in a few rotor revolutions.

The two types of waves as detected experimentally by six circumferentially distributed hot-wires [9] are displayed in Fig. 2. As can be observed from these pressure signals, modal and spike stall are characterized by a very different dynamic behavior. Modal perturbations can have from 1 to 6–10 circumferential lobes, and rotate at a fraction of the shaft speed ($\sim 10 - 40\%$). On the contrary, spike perturbations were found to rotate much faster, at around $\sim 70 - 90\%$ of the rotational speed. This was in agreement with the intuitions of Emmons et al. [4], who attributed the rotational speed of the disturbance to the inertia of the stalled region. As the volume of the stalled portion decreases, the ratio of pressure forces to mass increases. This leads to perturbations whose rotational rate approaches that of the shaft.

The critical mass flowrate at which rotating stall and surge occur can be well predicted experimentally. Full annulus unsteady CFD simulations also provide accurate results [12–16], but their use is still limited due to the high computational cost. Several reduced order models (ROM) have been developed over the years to predict the onset of instabilities at low cost. Greitzer [3] proposed a lumped parameters model capable of determining the occurrence of surge in a compression system. The rotating stall problem was tackled by Moore [17–19], who modeled the evolution of circumferential inlet perturbations in the machine through incompressible two-dimensional (2D) linearized equations applied to each subcomponent. Coupling together the different compressor components, he derived an eigenvalue problem (EVP), whose solution provides the onset of rotating stall waves. Moore and Greitzer subsequently developed a unified model [20,21], capable of describing the onset, growth, and interaction of stall and surge-like perturbations.

A semi-empirical model for low-speed radial compressors has been proposed by Senoo and Kinoshita [22]. The model correlates

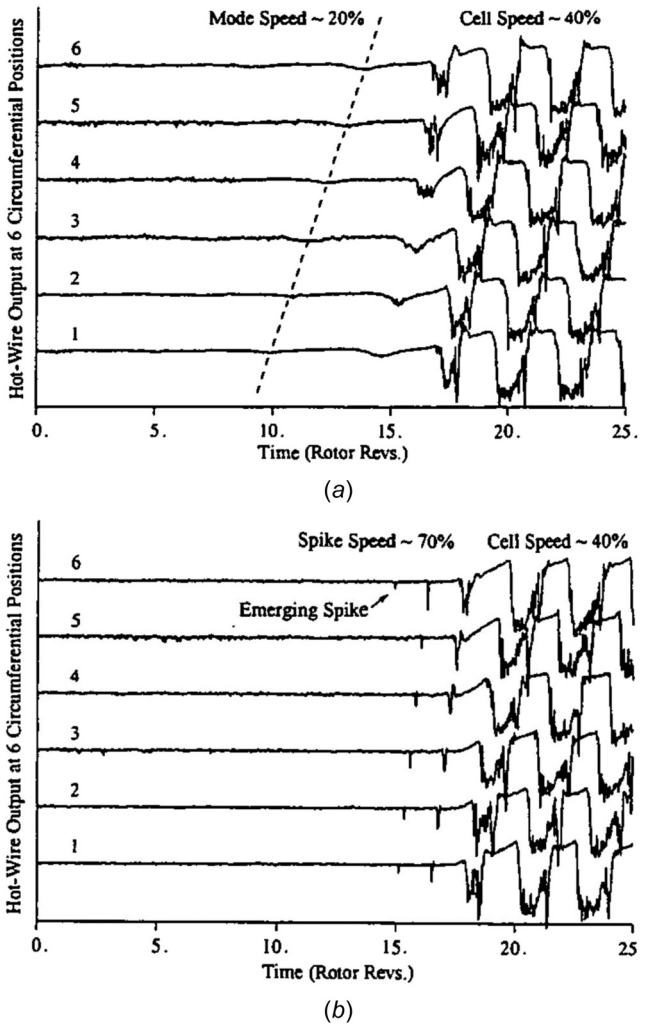

Fig. 2 Modal stall (top) and spike stall (bottom) hot-wire readings, from Camp and Day [9]

the rotating stall limit with the flow angle at the diffuser inlet and the geometrical characteristics of the machine. At those critical conditions, the radially outwards momentum of the slow particles in the boundary layer is not large enough to overcome the adverse pressure gradient, leading to flow reversal and large-scale instability. The applicability of the model to high-speed compressors has not been assessed yet.

Research carried out at MIT in the 1990s led to the conception and development of more accurate models. Bonnaure [23] modeled instabilities in high-speed axial compressor stages by solving the 2D linearized compressible flow perturbation equations. Feulner [24] extended the model in the frequency domain to be suitable for control purposes. A milestone in the modeling of flow instabilities in centrifugal compressors was reached by Spakovszky [25–27], who developed a 2D incompressible model capable of accurately predicting modal stall inception in low-speed axial and radial machines. The main flaw of the model is arguably its inaccuracy to deal with compressibility and spike-stall phenomena.

Gong [28,29] proposed a three-dimensional (3D) compressible flow model able to predict modal and spike-stall phenomena. It is based on the numerical simulation of the unsteady Euler equations augmented with body forces (BFM), a concept initially proposed by Marble [30]. The use of body forces makes the model computationally efficient, as the mesh can be coarse due to the absence of the physical blades in the domain. Gong [28,29] showed that the model was able to predict spike stall solely in axial machines, and its accuracy was found to be highly dependent on the formulation of the

body forces. Because of this reason, more accurate BFM were conceived by, e.g., Chima [31] and then Longley [32], who added the blade metal blockage factor into the BFM formulation. Benneke [33] and Kottapalli [34] developed BFM models specifically tailored to centrifugal compressors; however, their application to stall predictions failed due to numerical instability issues. Other versions of BFM-based flow models for compressor stall simulations were proposed by Righi et al. [35–38], Ji et al. [39], and Zheng et al. [40].

More recently, Sun et al. [41] applied the global instability theory [42] to turbomachinery flows. The approach revolves around a BiGlobal stability analysis of the circumferentially averaged solution of a single-passage Reynolds-averaged Navier–Stokes (RANS) simulation. Liu et al. [43], Yunfei et al. [44], Sun et al. [45], Hu et al. [46], He et al. [47], Xie et al. [48,49], and Xu et al. [50,51] extended the model and applied it to stall prediction in axial and radial high-speed machines. In the investigated cases, the results of the model provided a value of the critical mass flowrate within 2% of the experimental datum. In addition, the model accuracy was found to be unaffected by the choice of the turbulence closure used for the computation of the base flow [49].

With the abundance of available models, there arises the need of understanding their suitability for the design of high-speed radial compressors. This review provides a comprehensive discussion of the strengths and limitations of the various modeling approaches. Considerations on the appropriate model selection are discussed. Two models that appear particularly promising, namely, those of Spakovszky and Sun, are detailed and applied to exemplary flow instability problems.

2 Methodologies for Instabilities Prediction

The various numerical models for predicting flow instabilities in compressors can be grouped in three main categories:

- High-fidelity unsteady CFD modeling (HiFi-CFD)
- Reduced-order unsteady CFD modeling (ROM-CFD)
- Linearized stability analysis (LSA)

The use of the occurrence of periodic oscillations in the residuals of RANS simulations as a criterion for the onset of instabilities is here not considered as a further method, since the results can be highly dependent on the turbulence model and numerical settings [52].

2.1 High-Fidelity Unsteady Computational Fluid Dynamics Modeling. In the context of compressor instability, HiFi-CFD refers to full annulus unsteady Reynolds-Averaged Navier–Stokes (URANS) simulations, large eddy simulations (LES) or hybrid RANS-LES approaches. The whole machine needs to be meshed since the rotating stall perturbations break the circumferential periodicity of the compressor geometry, which renders single-passage simulations unsuitable. The mesh needs to guarantee an accurate resolution of the boundary layers, and the simulated time interval should span several rotor revolutions. This class of very accurate methods is suited to validate results from reduced order models or to investigate the physics of the instability phenomena.

The choice of the turbulence model depends on the level of details required. Rotating stall is a phenomenon triggered by local separations, where an accurate resolution of the boundary layer is fundamental. Several authors obtained good accuracy of the critical mass flowrate using URANS modeling [12–16]. As a result, this approach should be the first to be employed, followed eventually by LES in case a higher level of details of the small-scale effects is required.

If the simulation of surge phenomena is of concern, the compressor CFD domain must be coupled with other system components to provide realistic dynamic boundary conditions. Ji et al. [39] and Huang et al. [53] describe how such coupling may be established using reduced order models for the other system components. On the other hand, one can simulate stall events by exclusively focusing on the compressor and treating it as if it were decoupled from the system.

To predict the critical mass flowrate, different simulation strategies can be used. The first option is to perform a simulation at a near stall mass flowrate until statistical steadiness is achieved. At this point, the mass flowrate is reduced, and the process is repeated until the instability shows up spontaneously in the domain. This method requires extensive computational resources since many simulations must be performed for several rotor revolutions.

An alternative strategy is to artificially force perturbations at the most critical location. The force should be of minimal magnitude, brief in duration, and designed to excite the maximum possible number of fluid modes. This method allows reducing the cost of each simulation since the perturbations are directly excited. An example of the usable perturbation shape is provided by the 3D short-scale force impulse described by Gong [28].

Another alternative numerical methodology for reducing the computational cost is to promote local flow separation by increasing the effective stagger angle of a single blade. Pullan et al. [12] investigated spike-stall mechanisms in the NASA E^3 rotor using URANS simulations with the Spalart–Allmaras (SA) turbulence model. They increased the stagger angle of one blade by 1 deg, setting the spike location. They compared the results of 3D and 2D simulations, and they found matching results, leading to the conclusion that the small-scale effect can be neglected once large-scale flow separations emerge.

A similar approach was employed by Dodds and Vahdati [15], who studied the behavior of an eight-stage high-speed compressor during slow acceleration maneuvers with URANS modeling. They induced a mismatch in the front stages by adjusting the variable stator vanes, thereby reducing the time required for the rotating stall to form.

Large eddy simulations modeling can be applied to investigate the effects of broadband and small-scale flow structures on the stall process. Sündstrom et al. [54,55] used LES to investigate the surge and rotating stall characteristics of a turbocharger for automotive applications. They analyzed the correlation between the instability inception and evolution with the main blading characteristics, such as the instantaneous incidence and loading. Proper orthogonal decomposition was employed to extract the most energetic flow structures during surge and stall events, revealing the underlying physics of the process.

In conclusion, high-fidelity CFD is versatile and applicable to various compressor types and fluid scenarios, and limited primarily by the available computational resources. It also serves as an effective tool to evaluate nonlinear effects, to scrutinize local details, and to validate ROM.

2.2 Reduced-Order Unsteady Computational Fluid Dynamics Modeling. To reduce the computational cost of HiFi-CFD, Gong [28] proposed to solve the full-annulus incompressible Euler axisymmetric equations with the use of a BFM

$$\left(\frac{\partial}{\partial t}+\Omega\frac{\partial}{\partial\Omega}\right)\begin{bmatrix}0\\ ru_z\\ ru_\theta\\ ru_r\end{bmatrix}+\frac{\partial}{\partial z}\begin{bmatrix}ru_z\\ ru_z^2+rp/\rho\\ ru_\theta u_z\\ ru_r u_z\end{bmatrix}+\frac{\partial}{\partial r}\begin{bmatrix}ru_r\\ ru_z u_r\\ ru_\theta u_r\\ ru_r^2+rp/\rho\end{bmatrix}=\begin{bmatrix}0\\ F_z\\ u_\theta u_r+F_\theta\\ u_\theta^2+p/\rho+F_r\end{bmatrix} \tag{1}$$

where $\rho, u_r, u_\theta, u_z, \rho$ are the density, absolute velocity components, and pressure. F_r, F_θ, F_z are the components of the body force, and Ω is the shaft angular velocity, which serves to formulate the equations in the stationary frame for the rotating blocks. The BFM allows to drastically reduce the computational cost since the mesh does not need to resolve the blades and the associated boundary layers. In

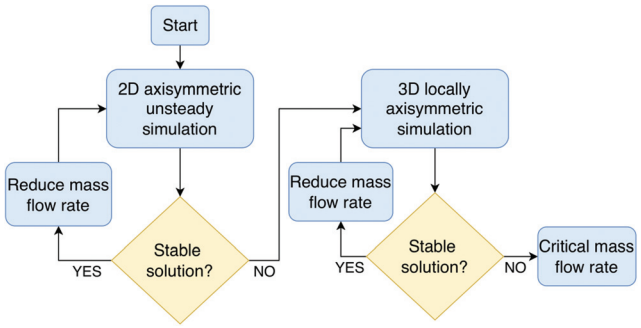

Fig. 3 ROM-CFD workflow

addition, simulation time-step can be larger as in HiFi-CFD. For this modeling approach, an example of simulation workflow is given in Fig. 3.

In Gong's original work, the body force was expressed in relation to the pressure-turning characteristics of the blade, as derived from experimental data. In alternative versions, however, the model coefficients are calibrated using the results of single-passage RANS simulations. Perturbations were promoted by the inclusion of a short-scale 3D disturbance at the blade tip, and both spike and modal waves were successfully predicted in axial compressors.

Many evolutions of this technique are available in the literature, with the main differences resulting from the chosen fidelity level of the governing equations and the calibration data type of the BFM. Several references for these works can be found in the introduction.

In summary, ROM-CFD models are adequate for predicting the instability limit of low and high-speed compressors to finite amplitude perturbations. Their drawbacks include higher computational cost compared to LSA models and lower accuracy compared to HiFi-CFD. The accuracy of ROM-CFD models highly depends on the BFM.

2.3 Linearized Stability Analysis. Linearized stability analysis is a mathematical technique used to examine the response of a dynamic system to perturbations of infinitesimal amplitude. In the context of fluid flows in compressors, LSA can be used to analyze the stability characteristics of the fluid system when perturbed around a steady-state condition, corresponding to a stable operating point of the machine. The dynamics of a time-invariant nonlinear system without external forcing can be expressed by the general governing equations

$$\dot{\mathbf{x}} = \mathbf{f}(\mathbf{x}) \tag{2}$$

where $\mathbf{x}$ denotes the state space vector and $\mathbf{f}$ the nonlinear governing equations. The specific state vector and equations vary depending on the employed model. The state vector generally corresponds to the primitive flow variables $\mathbf{x} = [\rho, \mathbf{u}, p]^{\mathrm{T}}$, and $\mathbf{f}$ represents the Navier–Stokes equations. Under the assumption of small amplitude perturbations around an equilibrium point (e.g., a steady compressor operating point), the equations can be linearized and written as

$$\dot{\mathbf{x}}' = \left.\frac{\partial \mathbf{f}}{\partial \mathbf{x}}\right|_{\mathbf{x}_0} \cdot \mathbf{x}' = \mathbf{A} \cdot \mathbf{x}' \tag{3}$$

where $\mathbf{x}_0$ denotes the equilibrium point, $\mathbf{x}' = \mathbf{x} - \mathbf{x}_0$ is the related perturbation vector, and $\mathbf{A}$ is the dynamic matrix of the system. The methods developed for compressor instabilities differ in the underlying governing equations and state space variables, but they all result in an EVP whose solution provides the stability characteristics of the system.

The models within this category cover a broad spectrum of fidelity levels, and the choice should be tailored to the particular application. From a qualitative perspective, a smaller dimension of the state space vector translates to reduced computational costs, increased modeling weight, and increased sensitivity of results to model parameters. The primary strength of these models lies in their computational efficiency relative to the other two classes, rendering them well-suited for investigating the design space of innovative compressors with the goal of expanding their operating range.

Sections 2.3.1–2.3.3 provide a comprehensive description of three LSA-based models of increasing complexity and accuracy: the Greitzer Model, the Spakovszky Model, and the Sun Model.

2.3.1 The Greitzer Model. Every compression system can be represented by an equivalent model consisting of the components represented in Fig. 4. Greitzer assumed a lumped parameter approach, with a uniform inviscid incompressible flow in the ducts, and a compressible plenum where isentropic transformations take place. He introduced the parameters

$$\begin{cases} B = \dfrac{u}{2a}\sqrt{\dfrac{V_p}{A_c L_c}} \\ G = \dfrac{L_t A_c}{L_c A_t} \end{cases} \tag{4}$$

where u is the flow velocity in the compressor duct, $a = \sqrt{\gamma RT}$ is the speed of sound, V_p is the plenum volume, and A_c, L_c, A_t, L_t are the area and length of the compressor and throttle ducts. The governing equations can be written in nondimensional form as

$$\begin{cases} \dfrac{d\phi_c}{d\xi} = B\left(\psi_c(\phi_c, \Omega) - \psi_p\right) \\ \dfrac{d\phi_t}{d\xi} = \dfrac{B}{G}\left(\psi_p - \psi_t(\phi_t)\right) \\ \dfrac{d\psi_p}{d\xi} = \dfrac{1}{B}\left(\phi_c - \phi_t\right) \end{cases} \tag{5}$$

where $\mathbf{x} = [\phi_c, \phi_t, \psi_p]^{\mathrm{T}}$ is the state vector comprised by flow coefficients in the compressor and throttle ducts, and by the nondimensional plenum pressure. $\xi = \mathrm{ta}\sqrt{\frac{A_c}{V_p L_c}}$ is the nondimensional time, $\psi_c(\phi_c, \Omega)$ and $\psi_t(\phi_t)$ are the compressor and throttle characteristics, specific for each system. The characteristic polynomial of Eq. (5) is given by

$$s(\lambda) = -\lambda^3 + \lambda^2\left(B\psi'_{c_0} - \frac{B\psi'_{t_0}}{G}\right) + \lambda\left(\frac{B^2\psi'_{c_0}\psi'_{t_0}}{G} - \frac{1}{G} - 1\right) + \left(\frac{B\psi'_{c_0}}{G} - \frac{B\psi'_{t_0}}{G}\right) \tag{6}$$

where the slopes of the characteristics are evaluated at the operating point. If all the three roots of Eq. (6) have negative real part, the system is stable to small surge-like perturbations. The result can be

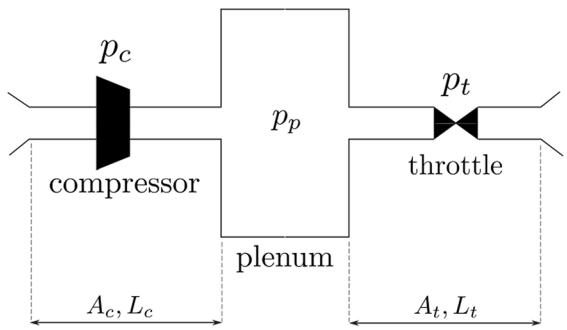

Fig. 4 Sketch of the Greitzer model compression system

used to alter the B and G characteristics of the system during the design process to enhance stability.

2.3.2 The Spakovszky Model. The underlying idea is to solve simplified perturbation equations for every component of a compressor in terms of the complex frequency s, and then connect the single transfer functions linking input to output perturbations. These modular characteristics enable easy implementation and flexibility of the model to treat different kinds of compressors.

The model is based on the assumption of uniform 2D perturbations along the blade span, incompressibility of the baseflow, and exploits a semi-actuator disk model for modeling the components acting on the flow (e.g., bladed rows and impeller). The state vector utilized in the analysis is given by $\boldsymbol{x}' = [u'_z, u'_\theta, p']^{\mathrm{T}}$ for the axial stations (e.g., the inlet of a radial impeller) or $[u'_r, u'_\theta, p']^{\mathrm{T}}$ for the radial ones (e.g., the outlet of a radial impeller). Expressions for the transfer functions of every component (e.g., inlet duct, rotor rows, stator rows, etc.…) are given in Ref. [25]. The transfer functions connect the output to the input n-th circumferential harmonic perturbation

$$\mathbf{x}'_2 = \sum_{n=0}^{\infty} \mathbf{B}_n \cdot \mathbf{x}'_{1,n} \tag{7}$$

where $\mathbf{B}_n$ is the n-th circumferential harmonic transfer function of the specific component, and 1, 2 refers to the input and output stations. For the inlet and outlet domains, the transfer functions connect the perturbations at a given location and the fundamental modes present in the domain

$$\mathbf{x}' = \sum_{n=0}^{\infty} \mathbf{T}_n \cdot \begin{bmatrix} A(s) \\ B(s) \\ C(s) \end{bmatrix}_n \tag{8}$$

where $\mathbf{T}_n$ is the n-th transfer function of the specific inlet or outlet domain, and $A_n(s), B_n(s), C_n(s)$ refers to the n-th two pressure and vorticity waves. Considering, as an example, the vaned centrifugal compressor of Fig. 5, the n-th system transmission matrix can be expressed as

$$\begin{aligned} \mathbf{X}_{\mathrm{sys},n}(s) = {} & \mathbf{T}^{-1}_{\mathrm{ax},n}(z_4, s) \cdot \mathbf{B}_{\mathrm{dif},n}(s) \\ & \cdot \mathbf{B}_{\mathrm{vlsd},n}(s) \cdot \mathbf{B}_{\mathrm{imp},n}(s) \cdot \mathbf{T}_{\mathrm{ax},n}(z_1, s) \end{aligned} \tag{9}$$

where $\mathbf{T}_{\mathrm{ax},n}$, $\mathbf{B}_{\mathrm{dif},n}$, $\mathbf{B}_{\mathrm{vlsd},n}$, $\mathbf{B}_{\mathrm{imp},n}$ are respectively the n-th transfer functions for an axial duct, a vaned diffuser, a vaneless diffuser and a radial impeller. $\mathbf{X}_{\mathrm{sys},n}(s)$ is defined through the relation

$$\begin{bmatrix} A(s) \\ B(s) \\ C(s) \end{bmatrix}_{\mathrm{dn},n} = \mathbf{X}_{\mathrm{sys},n}(s) \cdot \begin{bmatrix} A(s) \\ B(s) \\ C(s) \end{bmatrix}_{\mathrm{up},n} \tag{10}$$

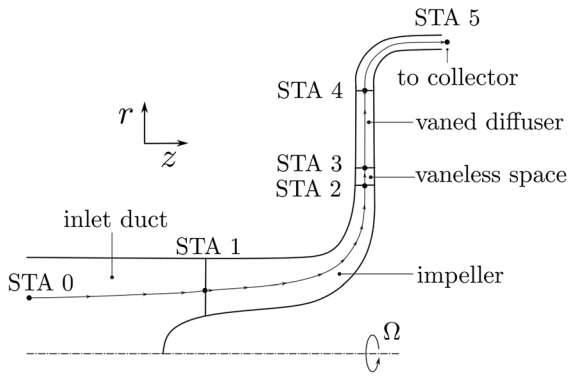

Fig. 5 Sketch of the NASA CC3 vaned centrifugal compressor, adapted from [25]

where up and dn refer to the far upstream and downstream locations with respect to the compressor.

The boundary conditions needed to close the problem are:

- Zero forward potential wave at STA1

$$B_n(s)\Big|_{\mathrm{up}} = 0 \tag{11}$$

- Zero vortical wave at STA1

$$C_n(s)\Big|_{\mathrm{up}} = 0 \tag{12}$$

- Zero backward potential wave at STA5

$$A_n(s)\Big|_{\mathrm{dn}} = 0 \tag{13}$$

Application of the boundary conditions results in the following homogeneous system:

$$\begin{bmatrix} \mathbf{EC} \cdot \mathbf{X}_{\mathrm{sys},n}(s) \\ \mathbf{IC} \end{bmatrix} \cdot \begin{bmatrix} A_n(s) \\ B_n(s) \\ C_n(s) \end{bmatrix}_{\mathrm{up}} = \begin{bmatrix} 0 \\ 0 \\ 0 \end{bmatrix}, \quad \forall n \geq 0 \tag{14}$$

where the exit and inlet boundary condition blocks are defined as

$$\mathbf{EC} = \left[\left(-\frac{s}{n} - \bar{u}_z^{\mathrm{dn}} - j\bar{u}_\theta^{\mathrm{dn}} \right) e^{nz_5}, \left(\frac{s}{n} - \bar{u}_z^{\mathrm{dn}} + j\bar{u}_\theta^{\mathrm{dn}} \right) e^{-nz_5}, 0 \right] \tag{15}$$

$$\mathbf{IC} = \begin{bmatrix} 0 & 1 & 0 \\ 0 & 0 & 1 \end{bmatrix} \tag{16}$$

To admit nontrivial solutions, the determinant of the coefficient matrix in Eq. (14) must be zero. Since the matrix is composed by transcendental functions of s, there is no indication of the number of roots. If one of the roots has a positive real part, the corresponding mode, if excited, will lead to instability, while the imaginary part describes its rotation rate. The critical mass flowrate is identified as the mass flowrate at which the first pole transitions into the positive real half-plane.

2.3.3 The Sun Global Instability Model. Rotating stall perturbations move along the annulus of the machine and remain confined in the computational domain while growing in amplitude. The baseflow field is 2π periodic in the circumferential direction and this makes BiGlobal temporal stability analysis suitable. The instability model developed by Sun [41] is a modification of the classical BiGlobal method developed for laminar to turbulent boundary layer transition. The physical plane used in the analysis is the meridional plane of the machine (z, r) and the θ coordinate is treated as a direction of invariance.

The starting point is the 3D Euler equations with a body force $\mathbf{F}$ to model the effects of the blades on the flow

$$\begin{cases} \dfrac{D\rho}{Dt} = -\rho \nabla \cdot \mathbf{u} \\ \rho \dfrac{D\mathbf{u}}{Dt} = -\nabla p + \rho \mathbf{F} \\ \rho \dfrac{De}{Dt} = -p \nabla \cdot \mathbf{u} + \rho W_F \end{cases} \tag{17}$$

where $\frac{D()}{Dt}$ refers to the material derivative, e to the total energy, and $\mathbf{F}$ to the body force. W_F is the work done by the body force on the flow. The equations are then linearly perturbed and written in the cylindrical reference frame of the machine. In compact form they read

$$\left(\mathbf{A}\frac{\partial}{\partial t}+\mathbf{B}\frac{\partial}{\partial r}+\mathbf{C}\frac{\partial}{r\partial\theta}+\mathbf{E}\frac{\partial}{\partial z}+\mathbf{R}+\mathbf{S}\right)\cdot\mathbf{x}'=0 \tag{18}$$

where the matrix $\mathbf{S}$ refers to the body force terms. The detailed perturbation Eq. (18) is given in appendix A for $\mathbf{x}'=[\rho',u_r',u_\theta',u_z',p']^{\mathrm{T}}$ as state vector.

The solution of Eq. (18) can be decomposed in the following series over all possible values of m and ω:

$$\mathbf{x}'(r,z,\theta,t)=\sum_{m,\omega}\tilde{\mathbf{x}}_{m\omega}(r,z)\cdot e^{-j(\omega t-m\theta)} \tag{19}$$

where m represents the circumferential mode number, ω is the complex frequency, $j^2=-1$, and $\tilde{\mathbf{x}}_{m\omega}(r,z)$ is the eigenfunction associated with a specific $[m,\omega]$ couple. Substituting the decomposition in Eq. (18) and considering every possible mode results in

$$\left(-j\omega\mathbf{A}+\mathbf{B}\frac{\partial}{\partial r}+\frac{jm}{r}\mathbf{C}+\mathbf{E}\frac{\partial}{\partial z}+\mathbf{R}+\mathbf{S}\right)\cdot\tilde{\mathbf{x}}=0 \tag{20}$$

where m,ω subscripts have been dropped for convenience. Equation (20) represents an eigenvalue problem, where perturbations exist only for those modes having shape $\tilde{\mathbf{x}}_{m\omega}(r,z)\cdot e^{jm\theta}$, and fluctuating at ω, solution of the EVP. Equation (19) shows that for every eigenvalue $\omega=\omega_R+j\omega_I$:

- $\omega_R>0$ indicates rotation of the perturbation in the same direction of the shaft revolution, as it is usually experienced for compressors.
- $\omega_R<0$ implies a backward rotating mode, as it has been documented for some peculiar case of compressor pre-stall waves [56].
- $\omega_I>0$ denotes exponential growth of the perturbation amplitude in time, leading rapidly to a nonlinear transient and eventually to rotating stall and/or surge.
- $\omega_I<0$ indicates a stable mode that will decay if excited.

Given these considerations, the rotating speed (RS) and damping factor (DF) of the perturbations are defined as

$$\begin{cases}\mathrm{RS}=\dfrac{\omega_R}{m\Omega}\\ \mathrm{DF}=\dfrac{\omega_I}{m\Omega}\end{cases} \tag{21}$$

where Ω is the shaft angular rate. With this definition, RS defines the relative angular speed of the stall inception wave compared to the shaft. The ultimate goal of the analysis is to identify the eigenvalue with the largest DF that determines the stability margin of the compressor. The mass flowrate at which the first eigenvalue crosses the real axis sets the instability limit.

Equation (20) is discretized on a two-dimensional grid of the meridional flow passage. To improve the numerical accuracy, the physical grid in the (z,r) domain is mapped to a computational grid (ξ,η), where the differential operator is expressed with the Chebyshev-Gauss-Lobatto collocation method [57]. On this auxiliary grid, the nodes must be located on the Gauss–Lobatto points

$$\begin{cases}\xi_i=\cos\left(\dfrac{\pi i}{N_z-1}\right), & i=0,\ldots,N_z-1\\ \eta_j=\cos\left(\dfrac{\pi j}{N_r-1}\right), & j=0,\ldots,N_r-1\end{cases} \tag{22}$$

where N_z,N_r are the number of points along the streamwise and spanwise directions used in the physical domain. Equation (18) is then converted in

$$\left(-j\omega\mathbf{A}+\widehat{\mathbf{B}}\frac{\partial}{\partial\xi}+\frac{jm}{r}\mathbf{C}+\widehat{\mathbf{E}}\frac{\partial}{\partial\eta}+\mathbf{R}+\mathbf{S}\right)\cdot\tilde{\mathbf{x}}=0 \tag{23}$$

where the transformed axial and radial matrices are given by

$$\begin{cases}\widehat{\mathbf{B}}=\dfrac{1}{J}\left(\mathbf{E}\dfrac{\partial r}{\partial\eta}-\mathbf{B}\dfrac{\partial z}{\partial\eta}\right)\\ \widehat{\mathbf{E}}=\dfrac{1}{J}\left(\mathbf{B}\dfrac{\partial z}{\partial\xi}-\mathbf{E}\dfrac{\partial r}{\partial\xi}\right)\end{cases} \tag{24}$$

and J is the Jacobian of the transformation computed with finite differences

$$J=\frac{\partial z}{\partial\xi}\frac{\partial r}{\partial\eta}-\frac{\partial z}{\partial\eta}\frac{\partial r}{\partial\xi}\approx\frac{\Delta z}{\Delta\xi}\frac{\Delta r}{\Delta\eta}-\frac{\Delta z}{\Delta\eta}\frac{\Delta r}{\Delta\xi} \tag{25}$$

The ξ and η differentiation operators can now be expressed with the Chebyshev-Gauss-Lobatto collocation method, which results in

$$\left(-j\omega\mathbf{A}+\hat{\mathbf{B}}_d+\frac{jm}{r}\mathbf{C}+\hat{\mathbf{E}}_d+\mathbf{R}+\mathbf{S}\right)\cdot\tilde{\mathbf{x}}=0 \tag{26}$$

As shown in the Appendix B, the $\mathbf{S}$ matrix related to the body force perturbations can be expressed as

$$\mathbf{S}=\frac{\mathbf{S}^{ss}}{1+\tau(-j\omega+jm\Omega)} \tag{27}$$

where $\mathbf{S}^{\mathrm{ss}}$ denotes the steady-state BFM coefficient matrix, and τ is a time-delay constant representing the lag between the flow perturbations and their effect on the body force field.

By defining the matrix

$$\mathbf{J}=\hat{\mathbf{B}}_d+\frac{jm}{r}\mathbf{C}+\hat{\mathbf{E}}_d+\mathbf{R} \tag{28}$$

the nonlinear eigenvalue problem results in

$$\left(-j\omega\mathbf{A}+\mathbf{J}+\frac{\mathbf{S}^{\mathrm{ss}}}{1+\tau(-j\omega+jm\Omega)}\right)\cdot\tilde{\mathbf{x}}=0 \tag{29}$$

Multiplying with the denominator and rearranging the terms yields a quadratic EVP [58]

$$(\mathbf{L}_2\omega^2+\mathbf{L}_1\omega+\mathbf{L}_0)\cdot\tilde{\mathbf{x}}=0 \tag{30}$$

for the matrices

$$\begin{cases}\mathbf{L}_0=\mathbf{J}(1+jm\Omega\tau)+\mathbf{S}^{\mathrm{ss}}\\ \mathbf{L}_1=\mathbf{A}(m\Omega\tau-j)-j\tau\mathbf{J}\\ \mathbf{L}_2=-\tau\mathbf{A}\end{cases} \tag{31}$$

The definition of the generalized state vector $\tilde{\boldsymbol{\varphi}}=[\tilde{\boldsymbol{x}},\omega\tilde{\boldsymbol{x}}]^{\mathrm{T}}$ allows one to transform Eq. (30) in a generalized linear EVP

$$\mathbf{Y}\cdot\tilde{\boldsymbol{\varphi}}=\omega\mathbf{P}\cdot\tilde{\boldsymbol{\varphi}} \tag{32}$$

where

$$\mathbf{Y}=\begin{bmatrix}-\mathbf{L}_0 & 0\\ 0 & \mathbf{I}\end{bmatrix},\qquad \mathbf{P}=\begin{bmatrix}\mathbf{L}_1 & \mathbf{L}_2\\ \mathbf{I} & 0\end{bmatrix} \tag{33}$$

The eigenvalues of Eq. (32) can be solved by the implicitly restarted Arnoldi method in the ARPACK library [59]. Because the search should typically focus on the most unstable eigenmode, and its corresponding eigenvalue is expected in a region close to a value σ than can be estimated, a shift-and-invert strategy can be applied

$$\hat{\mathbf{Y}} \cdot \tilde{\boldsymbol{\varphi}} = \lambda \tilde{\boldsymbol{\varphi}} \tag{34}$$

where $\hat{\mathbf{Y}} = (\mathbf{Y} - \sigma\mathbf{P})^{-1}\mathbf{P}$, and $\lambda = 1/(\omega - \sigma)$. The computational cost of the model is determined by the eigenvalue solver, which scales with the cube of the number of grid nodes. Since the model performs a temporal stability analysis, where ω is the unknown eigenvalue and m is a prefixed circumferential harmonic, it is essential to consider all potential values of m when searching for the critical mode. However, this procedure can be simplified by recognizing that, in the context of compressor instabilities, $m = 1$ is always the critical harmonic, as demonstrated by Sun et al. [41]. Consequently, the prediction of instability limits requires solely to solve for $m = 1$.

2.4 Model Selection. The selection of the most appropriate model for predicting the critical mass flowrate necessarily involves a tradeoff between accuracy and computational cost. Based on the review of existing literature, the following considerations are made:

- The treatment of instabilities in high-speed compressors with models developed for low-speed machines leads to misleading results, especially in those machines affected by critical compressible modes. A quantitative analysis of the discrepancies is given by Liu et al. [43].
- Models that use semi-actuator disk strategies produce inaccurate results for spike-stall inception. These models assume that all the blades operate under the same flow conditions, which is unrealistic when spikes occur. The model limitations were demonstrated on the case of a high-speed compressor with vaned diffuser by Spakovszky and Roduner [60]. Modal-stall was successfully detected in cases with an open bleed valve, but the model failed to provide accurate results for spike-stall inception mechanisms, observed when the bleed valve was closed.

Given their relatively low computational cost and high accuracy, the Spakovszky model and the Sun model are deemed most suited for the flow analysis and design optimization of radial compressors. For this reason, two exemplary applications of these two models are documented in the following.

3 Applications

3.1 Spakovszky Model. The Spakovszky model has been applied to predict the stall mass flowrate of a high-speed radial compressor for inverse Rankine integrated systems (IRIS) [1]. The compressor operates with the refrigerant R1233zd(E), the external diameter of the impeller is 45 mm, and the range of rotational speed is from 68 to 94 krpm. The compressor layout and its calculated operating map are shown in Fig. 6.

The system transmission matrix for this problem can be expressed as

$$\mathbf{X}_{\text{sys},n}(s) = \mathbf{T}^{-1}_{\text{rad},n}(r_3, s) \cdot \mathbf{B}_{\text{vlsd},n}(s) \cdot \mathbf{B}_{\text{imp},n}(s) \cdot \mathbf{T}_{\text{ax},n}(z_1, s) \tag{35}$$

where $\mathbf{T}_{\text{rad},n}$ is the n-th transfer function for a swirling flow. The boundary conditions are given by

$$\mathbf{IC} = \begin{bmatrix} 0 & 1 & 0 \\ 0 & 0 & 1 \end{bmatrix}, \quad \mathbf{EC} = [0\,0\,1] \tag{36}$$

which correspond to an undisturbed flow at the impeller inlet and a volute discharge characterized by a zero backward potential wave. Figure 7 reports the growth factors for the speedlines of Fig. 6. From the results, a change of the critical circumferential mode from the second to the fourth harmonic at high rotational speeds is evident. Due to the absence of experimental reference data, the results obtained with the Spakovszky model are compared with those obtained with the Senoo model, see Fig. 8. The plot demonstrates

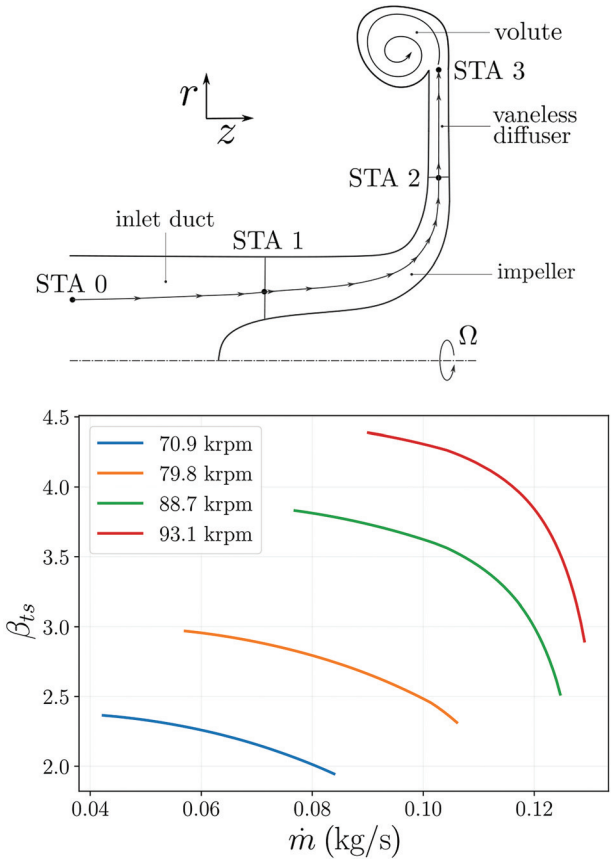

Fig. 6 Sketch of the IRIS compressor (top), and its characteristic curves (bottom)

that both models predict a qualitatively similar instability curve, namely, the line connecting the points on the speed-lines at which the onset of instabilities occurs. However, the instability curve predicted by the Spakovszky model is shifted rightward compared to the prediction of the Senoo model, and therefore predicts a reduced operating range of the compressor. It is important to note that these results can only quantify differences between the models. Both models have been derived for low-speed compressors, and it cannot be concluded that one is more accurate than the other for high-speed machines without further validation based on reliable reference data.

3.2 Sun Model. The accuracy and robustness of the Sun model is shown by comparing model predictions with the analytic solution for an annular-duct flow [45]. Consider a segment L of an infinitely long annular duct, with internal and external radii r_1, r_2, characterized by uniform axial velocity, pressure, and density fields. Assuming ideal gas behavior, the pressure perturbation satisfies the following equation:

$$(1 - M^2)\frac{\partial^2 p'}{\partial z^2} + \frac{\partial^2 p'}{r^2 \partial \theta^2} + \frac{\partial^2 p'}{\partial r^2} - \frac{1}{a^2}\frac{\partial^2 p'}{\partial t^2} - \frac{2M}{a}\frac{\partial^2 p'}{\partial z \partial t} + \frac{1}{r}\frac{\partial p'}{\partial r} = 0 \tag{37}$$

where a is the speed of sound and M is the axial Mach number. Using the method of separation of variables, the solution can be expressed as a series of modes

$$p'(r, \theta, z, t) = \sum R(r) e^{j(kz + m\theta + \omega t)} \tag{38}$$

where k is the axial wavenumber, m is the circumferential harmonic order, ω is the eigenfrequency, and $R(r)$ is the radial eigenfunction. Substituting Eq. (38) in Eq. (37) yields a Bessel equation of order m

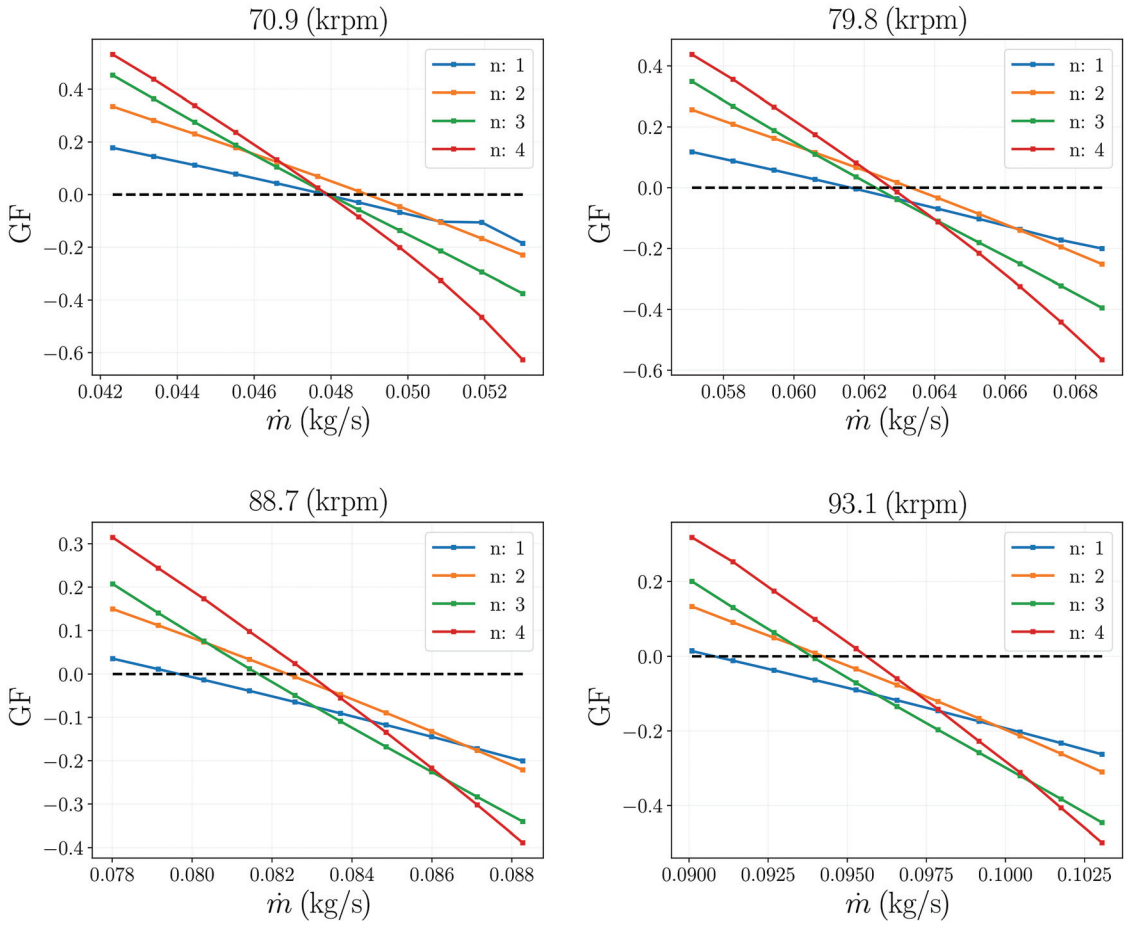

Fig. 7 Growth factors of the first 4 circumferential harmonics as a function of the mass flowrate at four different regimes

$$x^2R''(x) + xR'(x) + (x^2 - m^2)R(x) = 0 \tag{39}$$

where

$$\begin{cases} x = \lambda_{\text{mn}} r \\ \lambda_{\text{mn}}^2 = \left(\dfrac{\omega}{a} + k_{\text{mn}} M\right)^2 - k_{\text{mn}}^2 \end{cases} \tag{40}$$

for the circumferential m and radial n mode numbers.

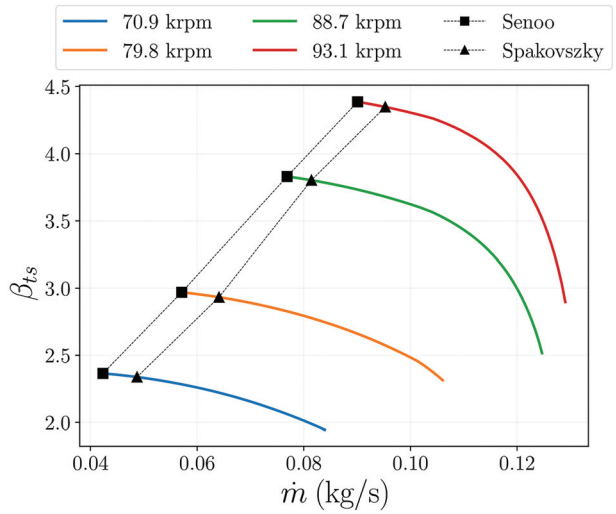

Fig. 8 IRIS compressor map, with Senoo and Spakovszky instability models predictions

The general solution of Eq. (39) is

$$R(r) = a_1 J_m(\lambda_{\text{mn}} r) + a_2 Y_m(\lambda_{\text{mn}} r) \tag{41}$$

where $J_m(x), Y_m(x)$ are the Bessel functions of order m of the first and second kind, and a_1, a_2 are two integration constants. Using the nonpenetration conditions at the duct walls

$$u_r'\Big|_{r_1,r_2} = 0 \Rightarrow \frac{\partial p'}{\partial r}\Big|_{r_1,r_2} = 0 \Rightarrow \frac{\partial R(r)}{\partial r}\Big|_{r_1,r_2} = 0 \tag{42}$$

leads to an eigenvalue problem for λ_{mn}

$$\begin{bmatrix} \dfrac{\partial}{\partial r} J_m(\lambda_{\text{mn}} r_1) & \dfrac{\partial}{\partial r} Y_m(\lambda_{\text{mn}} r_1) \\ \dfrac{\partial}{\partial r} J_m(\lambda_{\text{mn}} r_2) & \dfrac{\partial}{\partial r} Y_m(\lambda_{\text{mn}} r_2) \end{bmatrix} \cdot \begin{bmatrix} a_1 \\ a_2 \end{bmatrix} = \begin{bmatrix} 0 \\ 0 \end{bmatrix}$$

$$\Rightarrow \det \mathbf{Q}(\lambda_{\text{mn}}) = 0 \tag{43}$$

Figure 9 shows the first seven roots of Eq. (43) for $m = 1$ and the duct parameters of Table 1.

Substituting the results in Eq. (40) yields the eigenfrequencies

$$\omega_{\text{mn}\alpha} = a\sqrt{\left[(1 - M^2)\frac{\alpha\pi}{L}\right]^2 + (1 - M^2)\lambda_{\text{mn}}^2} \tag{44}$$

where α denotes the axial mode number (i.e., $k = \frac{\alpha\pi}{L}$, for $\alpha = 1, 2, \ldots, \infty$). The first eigenvalues for $m = 1$ are reported in

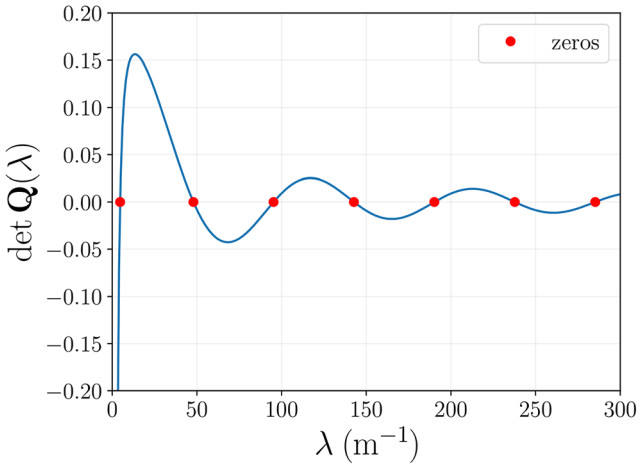

Fig. 9 First seven roots of Eq. (43) for the case of Table 1, with *m*=1

Table 1 Parameters of the annular duct test case

Input	Units	Value
Temperature	(K)	288
Pressure	(bar)	1
Mach number		0.015
Internal radius	(mm)	182.6
External radius	(mm)	248.7
Length	(mm)	80

Table 2 Natural frequencies of the modes [*m*, *n*, *α*]

m	n	α	ω (rad/s)
1	1	1	13,450
1	1	2	26,721
1	1	3	40,102
1	2	1	21,077
1	2	2	31,296
1	2	3	43,261
1	3	1	35,049
1	3	2	41,996
1	3	3	51,534

Table 2. Notice that all the eigenvalues are real numbers, due to the simplified assumptions that lead to zero damping and growth. In other words, the perturbations conserve their initial amplitude, pulsating at ω_R in time.

The same problem has been solved using the Sun model, discretizing the duct on a grid of 60×20 nodes in the axial and radial directions. Zero pressure perturbations have been set as boundary conditions at the duct ends and a nonpenetration velocity condition on the duct walls. The first five eigenfrequencies obtained are shown in Fig. 10, which demonstrates good agreement between numerical and analytical values.

The eigenfunction shapes were also analyzed. The analytical mode shape can be expressed as

$$\tilde{p}_{mn\alpha}(r,z) \propto R_{mn}(r) \cdot Z_\alpha(z) \tag{45}$$

where $Z_\alpha(z)$ is set by the zero pressure perturbation condition at the duct extremities $[0, L]$

$$Z_\alpha(z) \propto \sin\left(\frac{\alpha\pi z}{L}\right), \quad \alpha = 1, 2, \ldots, \infty \tag{46}$$

$R_{mn}(r)$ is obtained by combining Eqs. (41) and (43)

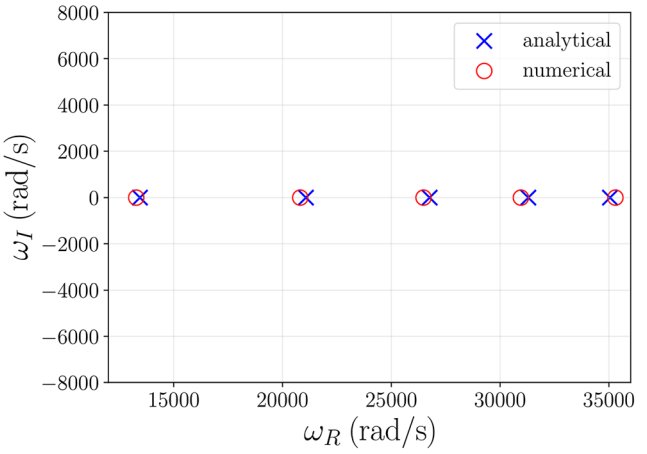

Fig. 10 Comparison between numerical and analytical eigenfrequencies for the annular duct case

$$R_{mn}(r) \propto J_m(\lambda_{mn} r) - \beta Y_m(\lambda_{mn} r), \quad m, n = 1, 2, \ldots, \infty \tag{47}$$

where β has been defined as

$$\beta = \frac{\partial[J_m(\lambda_{mn} r_1)]}{\partial r} \Big/ \frac{\partial[Y_m(\lambda_{mn} r_1)]}{\partial r} \tag{48}$$

Figure 11 shows the comparison between the numerical pressure eigenfunction and their analytical one-dimensional (1D)-slices, for the mode $[m, n, \alpha] = [1, 3, 3]$ at $\omega = 51350$ rad/s.

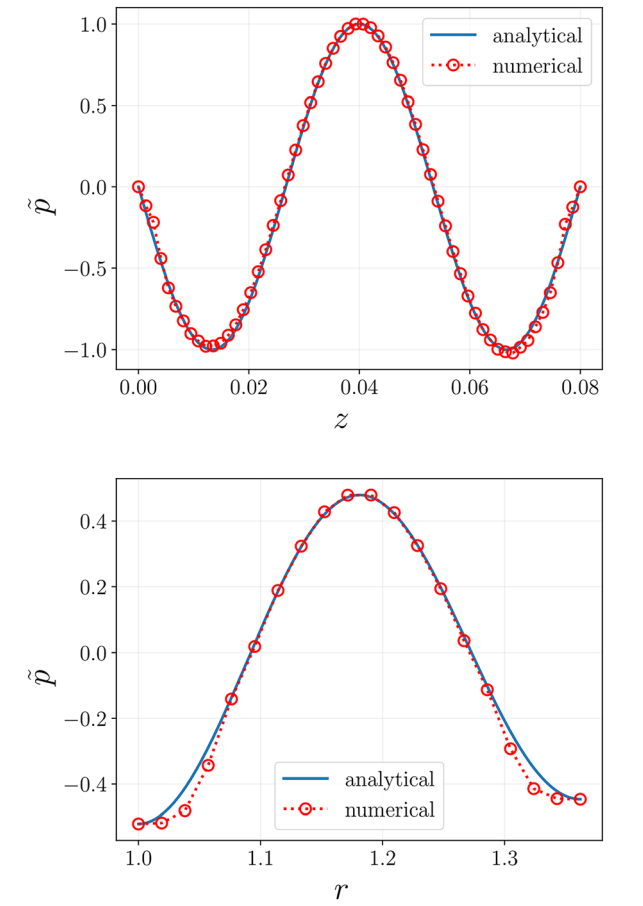

Fig. 11 Axial (top), and radial (bottom) slices of the numerical pressure eigenfunction for the mode [*m*, *n*, *α*]=[1, 3, 3]

Table 3 Settings used for the sensitivity study

	15 × 5	30 × 10	45 × 15	60 × 20
2	✓	✓	✓	✓
4		✓	✓	✓
6		✓	✓	✓
8			✓	✓
10			✓	✓

The columns represent different grid resolutions ($N_z \times N_r$), and the rows the order of the finite difference schemes.

Despite a qualitatively good agreement, the results provided by the Sun model deviate from the analytical reference close the boundaries of the domain. For this reason, a sensitivity study has been carried out and is documented in Sec. 3.2.1.

3.2.1 Sensitivity Study. The following numerical settings were identified to have the largest influence on the results of the Sun model:

- The grid resolution in the axial and radial directions;
- The finite difference order used for the Jacobian that relates the physical and computational grids.

Table 3 shows the parameters tested. The missing checkmarks indicate that the number of grid points is insufficient for the use of a particular finite difference scheme. For all the combinations tested, the relative error between the first five eigenvalues of the spectrum and the numerical results has been computed according to

$$\varepsilon_k = \frac{|\omega_k^N - \omega_k^A|}{\omega_k^A}, \quad k = 1, \ldots, 5 \tag{49}$$

where A and N stand for analytical and numerical values. The results were gathered in an error matrix, shown in Fig. 12.

The results indicate that the optimal settings are not characterized by a larger resolution, or a higher finite difference order, as it could be expected. In particular, the best settings for this case are 45_15_06 and 60_20_06. Due to this unexpected result, the accuracy of the grid Jacobian was analyzed to identify the error source.

Without loss of generality, consider the 1D grid transformation $x = x(\xi)$, where x and ξ are the physical and computational coordinates. For the i-th node of the grid

$$\begin{cases} x(i) = \dfrac{i}{N-1} \\ \xi(i) = \cos\left(\dfrac{i\pi}{N-1}\right) \end{cases} i = 0, 1, \ldots, N-1 \tag{50}$$

where the nodes along x are evenly spaced, the ones on ξ lie on the Gauss-Lobatto points, and N is the total number of points. The

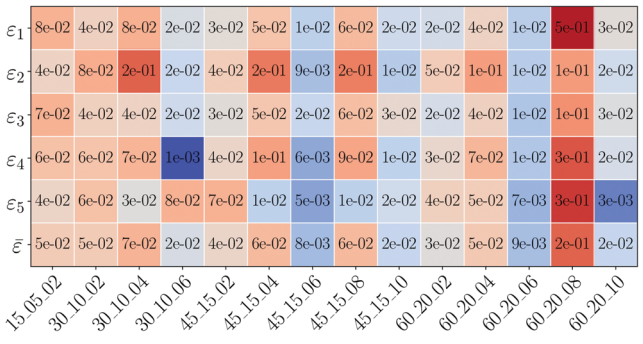

Fig. 12 Error matrix of the sensitivity study. The *x*-axis refers to the settings combinations according to the nomenclature (N_z_N_r_FDO). The last row summarizes the averaged relative error.

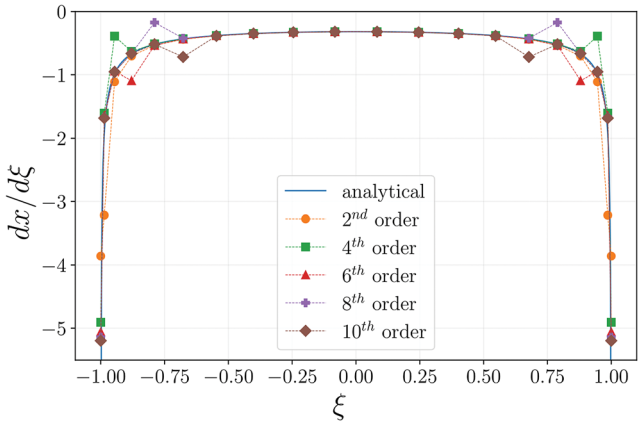

Fig. 13 Analytical and numerical gradients between a physical and a computational grid with 20 nodes

analytical transform and its derivative can be found eliminating i from the previous equations

$$\begin{cases} x = \dfrac{1}{\pi}\arccos\xi \\ \dfrac{dx}{d\xi} = -\dfrac{1}{\pi\sqrt{1-\xi^2}} \end{cases} \tag{51}$$

which present singularities of the derivative at the extremes of the computational domain $\xi = -1$ and $\xi = 1$. The comparison between analytical and numerical derivatives obtained with several finite difference schemes with order-of-convergence ranging from 2 to 10 is shown in Fig. 13.

High-order polynomials severely under or overshoot the analytical values near the extremities. Employing low-order

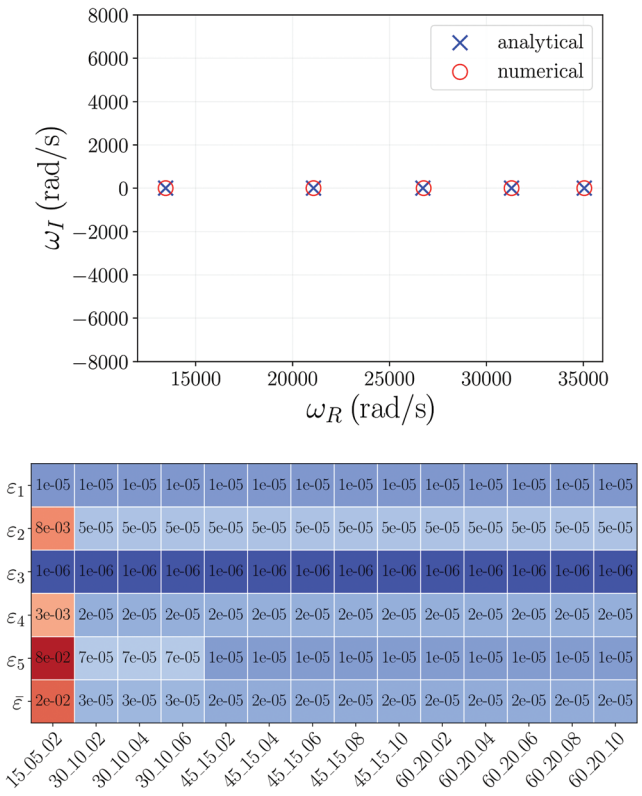

Fig. 14 Eigenvalues (top) and error matrix (bottom) for the annular duct flow discretized with the law given in Eq. (52)

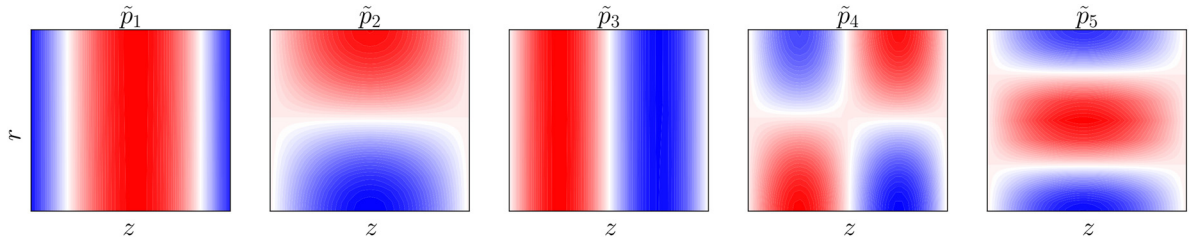

Fig. 15 First five pressure modes for the duct problem

differentiation schemes and increasing grid resolution does not resolve the issue. Instead, it leads to extremely large numerical values of the transformation gradients at the boundaries, thereby deteriorating the accuracy of the iterative Arnoldi eigensolver. As a result, there exists an optimal order of accuracy leading to the minimization in the error of the eigenvalues for a given grid resolution. This explains the results reported in Fig. 12, and the discrepancies observed in Fig. 11.

3.2.2 Alleviation of Numerical Model Errors. To alleviate the singularity problem in the grid Jacobian, we propose to employ an uneven distribution that closely resembles the Gauss-Lobatto distribution for generating the physical grid. Both axial and radial directions are discretized according to

$$x(i) = x_1 + (x_2 - x_1) \cdot \frac{1 - \cos\left(\frac{\pi i}{N-1}\right)}{2}, \quad i = 0, \ldots, N-1 \tag{52}$$

where x_1 and x_2 denote the first and last coordinates along the direction considered. Following the same approach used in Sec. 3.2.1, the transformation and the derivative are given by

$$\begin{cases} x = x_1 + (1 - \xi) \cdot \dfrac{x_2 - x_1}{2} \\ \dfrac{dx}{d\xi} = \dfrac{x_1 - x_2}{2} \end{cases} \tag{53}$$

and are not affected by singularities. Using this grid for the duct problem yields the eigenvalues shown in Fig. 14. The errors have been significantly reduced by at least two orders of magnitude. In addition, the results demonstrate grid-resolution independence, thereby verifying the correct implementation of the model. The numerical pressure eigenfunctions of the first five modes are shown in Fig. 15. As expected, the coarser configuration (15_05_02) shows larger errors for the modes $\tilde{p}_2$,$\tilde{p}_4$, and $\tilde{p}_5$ due to insufficient resolution in the radial direction.

For practical applications to realistic compressor geometries, it is challenging to define an analytical grid transformation. Nevertheless, the grid generation method can aim at clustering nodes toward the boundaries to emulate the distribution of Gauss-Lobatto points. This approach will arguably mitigate the most critical numerical errors introduced when solving the stability equations, ultimately yielding more accurate results.

4 Conclusion

Numerical models for estimating the critical mass flowrate have been reviewed and classified into three distinct groups. ROM-CFD and HiFi-CFD are considered the most appropriate for conducting in-depth analyses of instability modes, while LSA appears to be the optimal choice for predicting the operating range during the early design process. From the models falling within the LSA category, the Spakovszky model is deemed most accurate for predicting the critical mass flowrate in low-speed compressors, whereas the Sun model is considered more adequate for high-speed machines. Based on both literature and the findings of this study, the following conclusions are drawn:

- The rotating stall limit is the phenomenon on which the operating range prediction must be set. Surge is always preceded by stall-like perturbations, and its characteristics can be adequately modeled by the Greitzer model. Therefore any operating range calculation method should accurately predict the critical mass flow rate for rotating stall.
- LSA may not yield meaningful results for finite amplitude perturbations, such as radial or circumferential inlet distortions. The stability of finite amplitude perturbations should be studied with ROM-CFD or HiFi-CFD.
- The stability analysis conducted on the high-speed IRIS compressor demonstrates the good performance of the Spakovszky model for such machinery. The model accurately captures the expected trend of growth factors. A quantitative assessment of accuracy is pending; we encourage future studies that investigate the instability limit using HiFi-CFD and provide the required reference data.
- The analysis of the Sun model for a simple test case with an analytic solution has revealed a significant sensitivity of the results on numerical settings, particularly concerning grid resolution and the discretization scheme employed to transform the physical grid to the computational grid. While this problem has been solved for simple geometries with the approach given in Sec. 3.2.2, there are currently no general guidelines for selecting the most suitable discretization methods for complex compressor geometries.

Acknowledgment

The present work is financially supported by the Flow Physics and Technology department of TU Delft.

Data Availability Statement

The datasets generated and supporting the findings of this article are obtainable from the corresponding author upon reasonable request.

Appendix A: Perturbation Equations

Perturbing the flow variables of the continuity equation in cylindrical coordinates, and retaining terms up to the first order results in

$$\begin{aligned} &\frac{\partial \rho'}{\partial t} + \bar{u}_r \frac{\partial \rho'}{\partial r} + \bar{\rho} \frac{\partial u_r'}{\partial r} + \frac{1}{r}\left(\bar{u}_\theta \frac{\partial \rho'}{\partial \theta} + \bar{\rho} \frac{\partial u_\theta'}{\partial \theta}\right) \\ &+ \bar{u}_z \frac{\partial \rho'}{\partial z} + \bar{\rho} \frac{\partial u_z'}{\partial z} + \rho'\left(\frac{\partial \bar{u}_r}{\partial r} + \frac{\partial \bar{u}_z}{\partial z} + \frac{\bar{u}_r}{r}\right) \\ &+ u_r'\left(\frac{\bar{\rho}}{r} + \frac{\partial \bar{\rho}}{\partial r}\right) + u_z'\left(\frac{\partial \bar{\rho}}{\partial z}\right) = 0 \end{aligned} \tag{A1}$$

The radial perturbation momentum equation is

$$\frac{\partial u_r'}{\partial t}+\bar{u}_r\frac{\partial u_r'}{\partial r}+\frac{1}{\bar{\rho}}\frac{\partial p'}{\partial r}+\frac{\bar{u}_\theta}{r}\frac{\partial u_r'}{\partial \theta}+\bar{u}_z\frac{\partial u_r'}{\partial z}+\frac{\rho'}{\bar{\rho}^2}\frac{\partial \bar{p}}{\partial r}+u_r'\frac{\partial \bar{u}_r}{\partial r}+-2\frac{u_\theta'\bar{u}_\theta}{r}+u_z'\frac{\partial \bar{u}_r}{\partial z}=0 \tag{A2}$$

The tangential perturbation momentum equation is

$$\frac{\partial u_\theta'}{\partial t}+\bar{u}_r\frac{\partial u_\theta'}{\partial r}+\frac{1}{r}\left(\bar{u}_\theta\frac{\partial u_\theta'}{\partial \theta}+\frac{1}{\bar{\rho}}\frac{\partial p'}{\partial \theta}\right)+\bar{u}_z\frac{\partial u_\theta'}{\partial z}+u_r'\left(\frac{\partial \bar{u}_\theta}{\partial r}+\frac{\bar{u}_\theta}{r}\right)+\frac{u_\theta'\bar{u}_r}{r}+u_z'\frac{\partial \bar{u}_\theta}{\partial z}=0 \tag{A3}$$

The axial perturbation momentum equation is

$$\frac{\partial u_z'}{\partial t}+\bar{u}_r\frac{\partial u_z'}{\partial r}+\frac{\bar{u}_\theta}{r}\frac{\partial u_z'}{\partial \theta}+\bar{u}_z\frac{\partial u_z'}{\partial z}+\frac{1}{\bar{\rho}}\frac{\partial p'}{\partial z}+\frac{\rho'}{\bar{\rho}^2}\frac{\partial \bar{p}}{\partial z}+u_r'\frac{\partial \bar{u}_z}{\partial r}+u_z'\frac{\partial \bar{u}_z}{\partial z}=0 \tag{A4}$$

The enthalpy perturbation equation is expressed in terms of pressure and density, considering a constant $c_p=\frac{\gamma R}{\gamma-1}$

$$\begin{aligned}&-\frac{\gamma\bar{p}}{\bar{\rho}}\frac{\partial \rho'}{\partial t}+\frac{\partial p'}{\partial t}-\frac{\gamma\bar{p}\bar{u}_r}{\bar{\rho}}\frac{\partial \rho'}{\partial r}+\bar{u}_r\frac{\partial p'}{\partial r}\\&+\frac{1}{r}\left(-\frac{\gamma\bar{p}\bar{u}_\theta}{\bar{\rho}}\frac{\partial \rho'}{\partial \theta}+\bar{u}_\theta\frac{\partial p'}{\partial \theta}\right)-\frac{\gamma\bar{p}\bar{u}_z}{\bar{\rho}}\frac{\partial \rho'}{\partial z}+\bar{u}_z\frac{\partial p'}{\partial z}\\&+\frac{\rho'}{\bar{\rho}}\left(\bar{u}_r\frac{\partial \bar{p}}{\partial r}+\bar{u}_z\frac{\partial \bar{p}}{\partial z}\right)+u_r'\left(\frac{\partial \bar{p}}{\partial r}-\frac{\gamma\bar{p}}{\bar{\rho}}\frac{\partial \bar{\rho}}{\partial r}\right)\\&+u_z'\left(\frac{\partial \bar{p}}{\partial z}-\frac{\gamma\bar{p}}{\bar{\rho}}\frac{\partial \bar{\rho}}{\partial z}\right)+-\frac{\gamma p'}{\bar{\rho}}\left(\bar{u}_r\frac{\partial \bar{\rho}}{\partial r}+\bar{u}_z\frac{\partial \bar{\rho}}{\partial z}\right)=0\end{aligned} \tag{A5}$$

Appendix B: Body Force Model

Following the discussion given in Ref. [47], the blade force acting on the fluid is divided in a component $\mathbf{F}_t$ that guides the flow to follow the mean camber surface, and another component $\mathbf{F}_l$, which reproduces the drag and loss effects

$$\mathbf{F}=\mathbf{F}_t+\mathbf{F}_l \tag{B1}$$

The turning force is perpendicular in every point to the local mean camber surface, while $\mathbf{F}_l$ acts in the opposite direction of the relative velocity. Under the assumption of steady and axisymmetric flow, the tangential angular momentum equation gives

$$\frac{u_m}{r}\frac{\partial(ru_\theta)}{\partial m}=F_\theta \tag{B2}$$

where $u_m=\sqrt{u_r^2+u_z^2}$ denotes the meridional velocity along the streamsurface, $\frac{\partial()}{\partial m}$ refers to the directional derivative along u_m, and F_θ is the tangential component of the blade force.

The loss force calculation is based on the entropy production

$$Tu_m\frac{\partial s}{\partial m}=-\mathbf{w}\cdot\mathbf{F}_l \tag{B3}$$

where $\mathbf{w}=[u_r,u_\theta-\Omega r,u_z]^{\mathrm{T}}$ is the relative velocity vector, T is the static temperature, and s is the static entropy. The tangential component of the turning force is given by

$$F_{t,\theta}=F_\theta-F_{l,\theta} \tag{B4}$$

and reconstruct the force vectors as a function of the blade geometry. In order to obtain analytical expression for the force, the method proceeds as follows:

- the loss force is modeled as proportional to the square of the relative velocity magnitude

$$F_l=\alpha(u_r^2+w_\theta^2+u_z^2) \tag{B5}$$

  where $\alpha(r,z)$ is calibrated using single-passage RANS simulations.
- the magnitude of the turning force is assumed to be proportional to the local meridional velocity and relative tangential velocity

$$F_t=\beta u_m w_\theta \tag{B6}$$

  where $\beta(r,z)$ is the model coefficient, found using the base-flow results;

The body force perturbation $\mathbf{F}'$ is then modeled as a first-order system with time delay τ

$$\tau\left(\frac{\partial}{\partial t}+\Omega\frac{\partial}{\partial \theta}\right)\mathbf{F}'+\mathbf{F}'=\left(\frac{\partial \bar{\mathbf{F}}}{\partial \bar{u}_r}u_r'+\frac{\partial \bar{\mathbf{F}}}{\partial \bar{u}_\theta}u_\theta'+\frac{\partial \bar{\mathbf{F}}}{\partial \bar{u}_z}u_z'\right) \tag{B7}$$

where the right-hand-side term corresponds to the steady-state body force perturbation, and τ is the time-constant characterizing the delay, usually set equal to the blade-passage flow-through time. In the frequency domain the relation becomes

$$\widetilde{\mathbf{F}}=\frac{1}{1+\tau(-j\omega+jm\Omega)}\left(\frac{\partial \bar{\mathbf{F}}}{\partial \bar{u}_r}\tilde{u}_r+\frac{\partial \bar{\mathbf{F}}}{\partial \bar{u}_\theta}\tilde{u}_\theta+\frac{\partial \bar{\mathbf{F}}}{\partial \bar{u}_z}\tilde{u}_z\right) \tag{B8}$$

References

[1] Giuffre, A., Colonna, P., and Pini, M., 2022, "The Effect of Size and Working Fluid on the Multi-Objective Design of High-Speed Centrifugal Compressors," Int. J. Refrig., **143**, pp. 43–56.
[2] Wittrock, D., Junker, M., Beversdorff, M., Peters, A., and Nicke, E., 2020, "A Deep Insight Into the Transonic Flow of an Advanced Centrifugal Compressor Design," ASME J. Turbomach., **142**(9), p. 091004.
[3] Greitzer, E. M., 1976, "Surge and Rotating Stall in Axial Flow Compressors—Part I: Theoretical Compression System Model," ASME J. Eng. Power, **98**(2), pp. 190–198.
[4] Emmons, H. W., Pearson, C. E., and Grant, H. P., 1955, "Compressor Surge and Stall Propagation," ASME J. Fluids Eng., **77**(4), pp. 455–467.
[5] Day, I. J., 2016, "Stall, Surge, and 75 Years of Research," ASME J. Turbomach., **138**(1), p. 011001.
[6] Vacula, J., and Novotný, P., 2021, "An Overview of Flow Instabilities Occurring in Centrifugal Compressors Operating at Low Flow Rates," ASME J. Eng. Gas Turbines Power, **143**(11), p. 111002.
[7] Zhang, L., He, R., Wang, S., and Zhang, Q., 2020, "A Review of Rotating Stall in Vaneless Diffuser of Centrifugal Compressor," J. Therm. Sci., **29**(2), pp. 323–342.
[8] Greitzer, E. M., 1980, "Review—Axial Compressor Stall Phenomena," ASME J. Fluids Eng., **102**(2), pp. 134–151.
[9] Camp, T. R., and Day, I. J., 1997, "A Study of Spike and Modal Stall Phenomena in a Low-Speed Axial Compressor," ASME Paper No. 97-GT-526.
[10] Tryfonidis, M., Etchevers, O., Paduano, J. D., Epstein, A. H., and Hendricks, G. J., 1995, "Prestall Behavior of Several High-Speed Compressors," ASME J. Turbomach., **117**(1), pp. 62–80.
[11] Garnier, V. H., Epstein, A. H., and Greitzer, E. M., 1991, "Rotating Waves as a Stall Inception Indication in Axial Compressors," ASME J. Turbomach., **113**(2), pp. 290–301.
[12] Pullan, G., Young, A. M., Day, I. J., Greitzer, E. M., and Spakovszky, Z. S., 2015, "Origins and Structure of Spike-Type Rotating Stall," ASME J. Turbomach., **137**(5), p. 051007.
[13] Dehner, R., and Selamet, A., 2019, "Three-Dimensional Computational Fluid Dynamics Prediction of Turbocharger Centrifugal Compression System Instabilities," ASME J. Turbomach., **141**(8), p. 081004.
[14] Marconcini, M., Bianchini, A., Checcucci, M., Ferrara, G., Arnone, A., Ferrari, L., Biliotti, D., and Rubino, D. T., 2017, "A Three-Dimensional Time-Accurate Computational Fluid Dynamics Simulation of the Flow Field Inside a Vaneless Diffuser During Rotating Stall Conditions," ASME J. Turbomach., **139**(2), p. 021001.
[15] Dodds, J., and Vahdati, M., 2015, "Rotating Stall Observations in a High Speed Compressor—Part II: Numerical Study," ASME J. Turbomach., **137**(5), p. 051003.

[16] Choi, M., Smith, N. H. S., and Vahdati, M., 2013, "Validation of Numerical Simulation for Rotating Stall in a Transonic Fan," ASME J. Turbomach., **135**(2), p. 021004.
[17] Moore, F. K., 1984, "A Theory of Rotating Stall of Multistage Axial Compressors: Part I—Small Disturbances," ASME J. Eng. Gas Turbines Power, **106**(2), pp. 313–320.
[18] Moore, F. K., 1984, "A Theory of Rotating Stall of Multistage Axial Compressors: Part II—Finite Disturbances," ASME J. Eng. Gas Turbines Power, **106**(2), pp. 321–326.
[19] Moore, F. K., 1984, "A Theory of Rotating Stall of Multistage Axial Compressors: Part III—Limit Cycles," ASME J. Eng. Gas Turbines Power, **106**(2), pp. 327–334.
[20] Moore, F. K., and Greitzer, E. M., 1986, "A Theory of Post-Stall Transients in Axial Compression Systems: Part I—Development of Equations," ASME J. Eng. Gas Turbines Power, **108**(1), pp. 68–76.
[21] Greitzer, E. M., and Moore, F. K., 1986, "A Theory of Post-Stall Transients in Axial Compression Systems: Part II—Application," ASME J. Eng. Gas Turbines Power, **108**(2), pp. 231–239.
[22] Senoo, Y., and Kinoshita, Y., 1978, "Limits of Rotating Stall and Stall in Vaneless Diffuser of Centrifugal Compressors," ASME Paper No. 78-GT-19.
[23] Bonnaure, L. P., 1991, "Modelling High Speed Multistage Compressor Stability," Master's thesis, Massachusetts Institute of Technology, Cambridge, MA.
[24] Feulner, M. R., Hendricks, G. J., and Paduano, J. D., 1996, "Modeling for Control of Rotating Stall in High Speed Multi-Stage Axial Compressors," ASME J. Turbomach., **118**(1), pp. 1–10.
[25] Spakovszky, Z. S., 2000, "Applications of Axial and Radial Compressor Dynamic System Modeling," Ph.D. thesis, Massachusetts Institute of Technology, Cambridge, MA.
[26] Spakovszky, Z. S., Gertz, J. B., Sharma, O. P., Paduano, J. D., Epstein, A. H., and Greitzer, E. M., 2000, "Influence of Compressor Deterioration on Engine Dynamic Behavior and Transient Stall-Margin," ASME J. Turbomach., **122**(3), pp. 477–484.
[27] Spakovszky, Z. S., Weigl, H. J., Paduano, J. D., van Schalkwyk, C. M., Suder, K. L., and Bright, M. M., 1999, "Rotating Stall Control in a High-Speed Stage With Inlet Distortion: Part I—Radial Distortion," ASME J. Turbomach., **121**(3), pp. 510–516.
[28] Gong, Y., 1999, "A Computational Model for Rotating Stall and Inlet Distortions in Multistage Compressors," Ph.D. thesis, Massachusetts Institute of Technology, Cambridge, MA.
[29] Gong, Y., Tan, C. S., Gordon, K. A., and Greitzer, E. M., 1999, "A Computational Model for Short-Wavelength Stall Inception and Development in Multistage Compressors," ASME J. Turbomach., **121**(4), pp. 726–734.
[30] Marble, F. E., and Hawthorne, W. R., 1964, "Three-Dimensional Flow in Turbomachines," High Speed Aerodyn. Jet Propul., **10**(10), pp. 83–166.
[31] Chima, R. V., 2006, "A Three-Dimensional Unsteady CFD Model of Compressor Stability," ASMEDC, Barcelona, Spain, Report No. NASA/TM—2006-214117.
[32] Longley, J. P., 2007, "Calculating Stall and Surge Transients," ASME Paper No. GT2007-27378.
[33] Benneke, B., 2009, "A Methodology for Centrifugal Compressor Stability Prediction," Master's thesis, Massachusetts Institute of Technology, Cambridge, MA.
[34] Kottapalli, A. P., 2013, "Development of a Body Force Model for Centrifugal Compressors," Master's thesis, Massachusetts Institute of Technology, Cambridge, MA.
[35] Righi, M., Pachidis, V., Könözsy, L., and Pawsey, L., 2018, "Three-Dimensional Through-Flow Modelling of Axial Flow Compressor Rotating Stall and Surge," Aerosp. Sci. Technol., **78**, pp. 271–279.
[36] Righi, M., Pachidis, V., Könözsy, L., Zhao, F., and Vahdati, M., 2020, "Three-Dimensional Low-Order Surge Model for High-Speed Axial Compressors," J. Global Power Propul. Soc., **4**, pp. 274–284.
[37] Righi, M., Pachidis, V., and Könözsy, L., 2020, "On the Prediction of the Reverse Flow and Rotating Stall Characteristics of High-Speed Axial Compressors Using a Three-Dimensional Through-Flow Code," Aerosp. Sci. Technol., **99**, p. 105578.
[38] Righi, M., Pachidis, V., Könözsy, L., Giersch, T., and Schrape, S., 2022, "Experimental Validation of a Three-Dimensional Through-Flow Model for High-Speed Compressor Surge," Aerosp. Sci. Technol., **128**, p. 107775.
[39] Ji, J., Hu, J., Ma, S., and Xu, R., 2022, "A Computational Method of Rotating Stall and Surge Transients in Axial Compressor," Energies, **15**(14), p. 5246.
[40] Zeng, H., Zheng, X., and Vahdati, M., 2022, "A Method of Stall and Surge Prediction in Axial Compressors Based on Three-Dimensional Body-Force Model," ASME J. Eng. Gas Turbines Power, **144**(3), p. 031021.
[41] Sun, X., Liu, X., Hou, R., and Sun, D., 2013, "A General Theory of Flow-Instability Inception in Turbomachinery," AIAA J., **51**(7), pp. 1675–1687.
[42] Theofilis, V., 2011, "Global Linear Instability," Annu. Rev. Fluid Mech., **43**(1), pp. 319–352.
[43] Liu, X., Sun, D., and Sun, X., 2014, "Basic Studies of Flow-Instability Inception in Axial Compressors Using Eigenvalue Method," ASME J. Fluids Eng., **136**(3), p. 031102.
[44] Yunfei, M., Xiaohua, L., Sun, D., and Xiaofeng, S., 2015, "Numerical Prediction of Stall Inception in Centrifugal Compressor Using Eigenvalue Method," ASME Paper No. GT2015-42590.
[45] Sun, X., Ma, Y., Liu, X., and Sun, D., 2016, "Flow Stability Model of Centrifugal Compressors Based on Eigenvalue Approach," AIAA J., **54**(8), pp. 2361–2376.
[46] Hu, C., Liu, P., Zhu, X., Chen, H., and Du, Z., 2017, "A Numerical Approach to Predict the Rotating Stall in the Vaneless Diffuser of a Centrifugal Compressor Using Eigenvalue Method," J. Theor. Appl. Mech., **55**(2), p. 635.
[47] He, C., Ma, Y., Liu, X., Sun, D., and Sun, X., 2018, "Aerodynamic Instabilities of Swept Airfoil Design in Transonic Axial-Flow Compressors," AIAA J., **56**(5), pp. 1878–1893.
[48] Xie, Z., Liu, Y., Liu, X., Sun, D., Lu, L., and Sun, X., 2018, "Computational Model for Stall Inception and Nonlinear Evolution in Axial Flow Compressors," J. Propul. Power, **34**(3), pp. 720–729.
[49] Xie, Z., Liu, Y., Liu, X., Lu, L., and Sun, X., 2019, "Effect of RANS Method on the Stall Onset Prediction by an Eigenvalue Approach," ASME J. Fluids Eng., **141**(3), p. 031401.
[50] Xu, D., He, C., Sun, D., and Sun, X., 2020, "Analysis Method of Compressor Stability Based on Eigenvalue Theory," ASME J. Fluids Eng., **142**(7), p. 071204.
[51] Xu, D., He, C., Sun, D., and Sun, X., 2021, "Stall Inception Prediction of Axial Compressors With Radial Inlet Distortions," Aerosp. Sci. Technol., **109**, p. 106433.
[52] Denton, J. D., 2010, "Some Limitations of Turbomachinery CFD," ASME Paper No. GT2010-22540.
[53] Huang, Q., Zhang, M., and Zheng, X., 2019, "Compressor Surge Based on a 1D-3D Coupled Method – Part 1: Method Establishment," Aerosp. Sci. Technol., **90**, pp. 342–356.
[54] Sundström, E., 2017, "Flow Instabilities in Centrifugal Compressors at Low Mass Flow Rate," Ph.D. thesis, KTH Royal Institute of Technology, Stockholm, Sweden.
[55] Sundström, E., Semlitsch, B., and Mihăescu, M., 2018, "Generation Mechanisms of Rotating Stall and Surge in Centrifugal Compressors," Flow, Turbul. Combust., **100**(3), pp. 705–719.
[56] Spakovszky, Z. S., 2004, "Backward Traveling Rotating Stall Waves in Centrifugal Compressors," ASME J. Turbomach., **126**(1), pp. 1–12.
[57] Peyret, R., 2002, *Spectral Methods for Incompressible Viscous Flow* (Volume 148 of Applied Mathematical Sciences), Springer, New York.
[58] Fang, Y., Sun, D., Xu, D., He, C., and Sun, X., 2023, "Rapid Prediction of Compressor Rotating Stall Inception Using Arnoldi Eigenvalue Algorithm," AIAA J., **61**(8), pp. 3566–3578.
[59] Lehoucq, R. B., Sorensen, D. C., and Yang, C., 1998, *ARPACK Users' Guide, Software, Environments, and Tools*, Society for Industrial and Applied Mathematics, Philadelphia, PA.
[60] Spakovszky, Z. S., and Roduner, C. H., 2009, "Spike and Modal Stall Inception in an Advanced Turbocharger Centrifugal Compressor," ASME J. Turbomach., **131**(3), p. 031012.